



Antimony oxide hydrate ($\text{Sb}_2\text{O}_5 \cdot 3\text{H}_2\text{O}$) as a simple and high efficient photocatalyst for oxidation of benzene



Jing Chen, Zhangsen Chen, Xiaoyun Zhang, Xiaofang Li, Linhui Yu, Danzhen Li*

State Key Laboratory of Photocatalysis on Energy and Environment, Research Institute of Photocatalysis, Fuzhou University, Fuzhou, 350002, PR China

ARTICLE INFO

Article history:

Received 18 January 2017

Received in revised form 30 March 2017

Accepted 1 April 2017

Available online 2 April 2017

Keywords:

Photocatalysis

Benzene

Photocatalytic oxidation

Antimonic acid

Antimony oxide hydrate

ABSTRACT

The development of high efficient and inexpensive photocatalyst for oxidation of indoor gaseous benzene is a big challenge. In this paper, a simple compound containing only one metal element named antimony oxide hydrate ($\text{Sb}_2\text{O}_5 \cdot 3\text{H}_2\text{O}$) is prepared by a facile hydrolysis–oxidation method. The photocatalytic activity for oxidation of benzene over $\text{Sb}_2\text{O}_5 \cdot 3\text{H}_2\text{O}$ is investigated for the first time. The conversion ratio and mineralization of benzene are 35.0% and 55% over $\text{Sb}_2\text{O}_5 \cdot 3\text{H}_2\text{O}$, which are 3.5 and 5.5 times higher than that of P25. Reactive oxygen species, including $\text{O}_2^{\bullet-}$ and $\bullet\text{OH}$, are detected by ESR experiments. The large amount of $\text{O}_2^{\bullet-}$ and long lived $\bullet\text{OH}$ over antimony oxide hydrate is the main reason for its good photocatalytic activity, and it is also proved that both $\text{O}_2^{\bullet-}$ and $\bullet\text{OH}$ are mainly origin from oxygen reduction. We believe that this energy saving, inexpensive and high efficient photocatalyst has potential industrial application value.

© 2017 Elsevier B.V. All rights reserved.

1. Introduction

Benzene is one of the elementary petrochemicals. Although it is used primarily as a precursor to the chemicals with more complex structure, for example ethylbenzene, it is a human carcinogen [1]. The development of a new technology for elimination of indoor gaseous benzene is a big challenge. Photocatalytic oxidation (PCO) using TiO_2 , as a promising technology for elimination of benzene, has attracted considerable interest [2–20]. Compared to the catalytic combustion process performed at a high temperature (ca. 300 °C), PCO is usually operated in a mild condition [21]. However, some bottlenecks greatly hamper its extensive application for the removal of benzene using PCO of TiO_2 . One is the low quantum yield due to the fast recombination of photogenerated electrons and holes. The other is the deactivation of photocatalysts mainly due to the deposition of less reactive byproducts on the surface of TiO_2 . To improve the PCO quantum yield, the development of the alternatives of TiO_2 becomes an important research topic.

Recently, many photocatalysts have been reported to be active for oxidation of benzene in gaseous phase, such as stannate, germinate, oxyhydroxide, antimonate [21–31]. These ternary oxides with d^0 or d^{10} electronic structure have diffusive conduction band and the valence band, which are benefit for the transfer of

photogenerated carriers (electrons and holes) [32]. Besides, the distorted MO_6 ($\text{M}=\text{metal with } d^0 \text{ or } d^{10} \text{ electronic structure}$) octahedron formed in these ternary oxides are considered as the profitable factor for the separation of photogenerated carriers because of the existent of dipole moment [33]. On the other hand, vanadate/ TiO_2 composites (or heterojunction) are also a series of photocatalysts with high efficient [34–37]. However, all of these ternary oxides and vanadate/ TiO_2 composites contain at least two metal elements. In addition, hydrothermal process or the calcination is necessary during the preparation procedure. The above two drawbacks will increase the cost of production, which will hamper the application of these photocatalysts. To reduce the cost of the photocatalyst, we shift our attention to the simple compounds containing only one metal element. Although $\beta\text{-Ga}_2\text{O}_3$ is a photocatalyst with high efficiency, the calcination (at least 600 °C) is ineluctable for the preparation of $\beta\text{-Ga}_2\text{O}_3$ [38]. To our knowledge, no simple compound except Ga_2O_3 has been reported to have higher photocatalytic efficiency than that of P25 for oxidation of benzene in gaseous phase.

Recently, strontium antimonate with pyrochlore structure has been reported to be high efficient for photocatalytic oxidation of benzene [39]. Thus, it is valuable to reduce the preparation cost of antimonate. In this paper, the facile hydrolysis–oxidation method was used to prepare the antimony oxide hydrate photocatalyst (denote as AOH) which adopts the same structure with strontium antimonate, but it only contains one metal element. By tuning the temperature, reaction time and the volume of H_2O_2 , we find that

* Corresponding author.

E-mail addresses: dzli@fzu.edu.cn, danzli@126.com (D. Li).

the AOH can be synthesized in a wide range of condition. The conversion ratio and mineralization of benzene are used to describe the photocatalytic activity. The photocatalytic activity of the best sample is much higher than that of P25. Reactive oxygen species, including $O_2^{\bullet-}$ and $\bullet OH$, are detected by ESR experiments. The intensity and the lifetime of the $O_2^{\bullet-}$ and $\bullet OH$ are investigated. Base on the ESR data, the photocatalytic mechanism is briefly discussed.

2. Materials and experiments

2.1. Preparation of photocatalyst

The AOH samples were prepared by a hydrolysis–oxidation process [40]. In a typical procedure, Sb_2O_3 powder (5.0 g, Sinopharm Chemical Reagent Co., Ltd.) was stirred in deionized water (20 mL) at 70 °C, and then H_2O_2 (5 mL, 30 wt.%, Sinopharm Chemical Reagent Co., Ltd.) was added to the mixture dropwise. After 90 min reaction, the resulting slurry was centrifuged and finally dried in an oven at 80 °C overnight without any rinse. The synthesis condition will influence the property of AOH. Thus, the optimum condition for preparing AOH is investigated by the orthogonal test, which will be discussed in detail later in this paper.

2.2. Characterization of photocatalysts

The crystal structure of AOH was determined by X-ray diffraction (XRD) on a Bruker D8 Advance X-ray diffractometer operated at 40 kV and 40 mA with Ni-filtered Cu $K\alpha$ radiation ($\lambda = 0.154056$ nm). The 2 θ range of XRD patterns was from 10° to 80°, the scan step size was 0.02° and the residence time was 0.1 s. The determination of bulk chemical composition is conducted on an energy-dispersive X-ray spectrometer (EDS) attached on the field-emission scanning electron microscope (FSEM, HITACHI SU-8010) with accelerating voltage of 10 kV. The particle sizes and morphologies of samples were observed on a transmission electron microscope (TEM) operated at 200 kV (JEM-2010, JEOL, Japan), and the further confirmation of the crystallographic structures were conducted under

the mode of high-resolution transmission electron microscopy (HRTEM). The surface chemical components and states of samples were determined by using an X-ray photoelectron spectrometer (ESCALAB 250, Thermo Fisher Scientific, USA) with monochromatic Al $K\alpha$ X-ray beam (1486.69 eV), and with the pressure of sample analysis chamber under high vacuum (3×10^{-10} mbar). The Brunauer–Emmett–Teller (BET) surface areas of AOH were deduced from N_2 adsorption–desorption isotherms at 77 K, and the isotherms were recorded by using an Accelerated Surface Area and Porosimetry Analyzer (ASAP 3020, Micromeritics, USA) after degassing the samples at 150 °C for 3 h. The optical properties of AOH were recorded by UV–vis diffuse reflectance spectroscopy (DRS) on a UV–vis spectrophotometer (Cary–500, Varian Co.) with $BaSO_4$ as the reference.

2.3. Evaluation of photocatalytic activity

Photocatalytic oxidation of benzene was conducted in a fixed-bed tubular reactor with a continuous flow mode. The reactor is made of a quartz tube with a length of 230 mm and an inner diameter of 2 mm, which was surrounded by three 4 W UV lamps (Philips, TUV 4W/G4 T5 and the wavelength centered at 254 nm (Fig. S1)). The intensity of light is 21.174 mW/cm² which is measured by a spectrometer (Spectrilight TM III, International Light Technologies, USA). In a typical experiment, the photocatalyst (particle size 50–70 mesh) was packed into the quartz reactor and the filling length was 7.5 cm. Benzene vapor was supplied by a gas cylinder with a total flow rate of 20 mL min⁻¹ and a constant concentration of 250 ppm. The on-line monitoring of the concentration of benzene and CO_2 was performed on the gas chromatograph (Agilent 7890A) with a FID and a TCD detector, respectively. The conversion and the mineralization ratio of benzene were calculated according to the steady-state reaction data by Eqs. (1) and (2), respectively.

Conversion Ratio

$$= \frac{\text{The elimination of benzene at time } t}{\text{The initial concentration of benzene}} \times 100\% \quad (1)$$

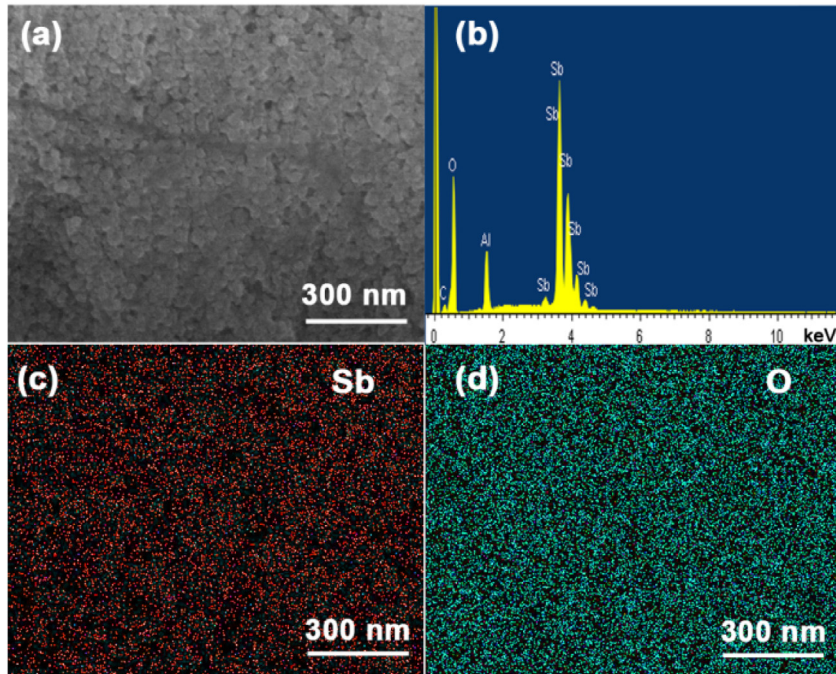


Fig. 1. The morphology of AOH (a). The EDS spectrum of AOH, The C and Al element signal stemmed from the electrically conductive double-sided adhesive tape (b). Elemental mapping of Sb (c) and O (d).

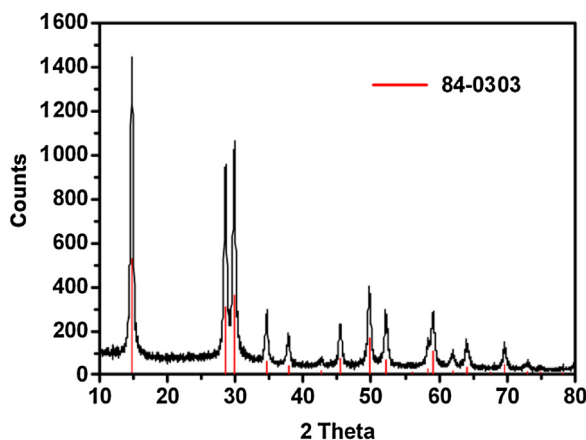


Fig. 2. The XRD pattern of AOH.

Mineralization Ratio

$$= \frac{\text{The concentration of CO}_2 \text{ at time } t}{6 \times \text{The elimination of benzene at time } t} \times 100\% \quad (2)$$

2.4. Measurement of reactive oxygen species

Reactive oxygen species (ROS) were detected by spin trapping technique using electron spin-resonance spectroscopies (ESR) (Bruker model A300 spectrometer) operated at 9.86 GHz with the microwave power 20 mW and 3512 Gs central magnetic field. The light source is one UV lamp with a wavelength centered at 254 nm (Philips, TUV 4W/G4 T5). The spin trapping agent 5,5-Dimethyl-1-pyrroline N-Oxide (DMPO) was used to verify the formation of superoxide and hydroxyl radicals. The ESR spectra were obtained from samples containing 3 mg AOH (or P25), 0.5 mL 50 mmol/L DMPO in methanol for super oxide radicals or water for hydroxyl radicals. To further distinguish the origin of ROS, superoxide dismutase (SOD, 600 U/ml) were employed to scavenge of super oxide.

2.5. Electrochemistry characterization

The flat band position of photocatalyst was obtained from Mott–Schottky (M–S) plots which were measured by using an electrochemical analyzer (CHI 660D) in a three-electrode cell at 1000 Hz with ac amplitude of 10 mV. The photocatalyst (AOH and P25) coated FTO glass, a platinum wire, a saturated calomel electrode and 0.1 M sodium sulfate were used as the working electrode, the counter-electrode, the reference electrode and the electrolyte, respectively.

3. Results and discussion

The morphology of AOH is shown in Fig. 1. AOH consists of irregular nanocrystals and only one metal Sb except the Al element signal stemmed from the electrically conductive double-sided adhesive tape. Both of the Sb and O are distributed uniformly in the selected area. The XRD pattern of AOH is shown in Fig. 2, which indicates that AOH has fine crystallinity and is a single phase of antimony oxide hydrate ($\text{Sb}_2\text{O}_5 \cdot 3\text{H}_2\text{O}$) according to JCPDS 84-0303. It adopts a pyrochlore-type structure (space group $\text{Fd}-3\text{m}$) [41,42]. The diffraction peaks of AOH at 14.8° , 28.5° , 29.8° , 34.6° and 45.4° are corresponding to the crystal planes (111), (311), (222), (400) and (511), respectively.

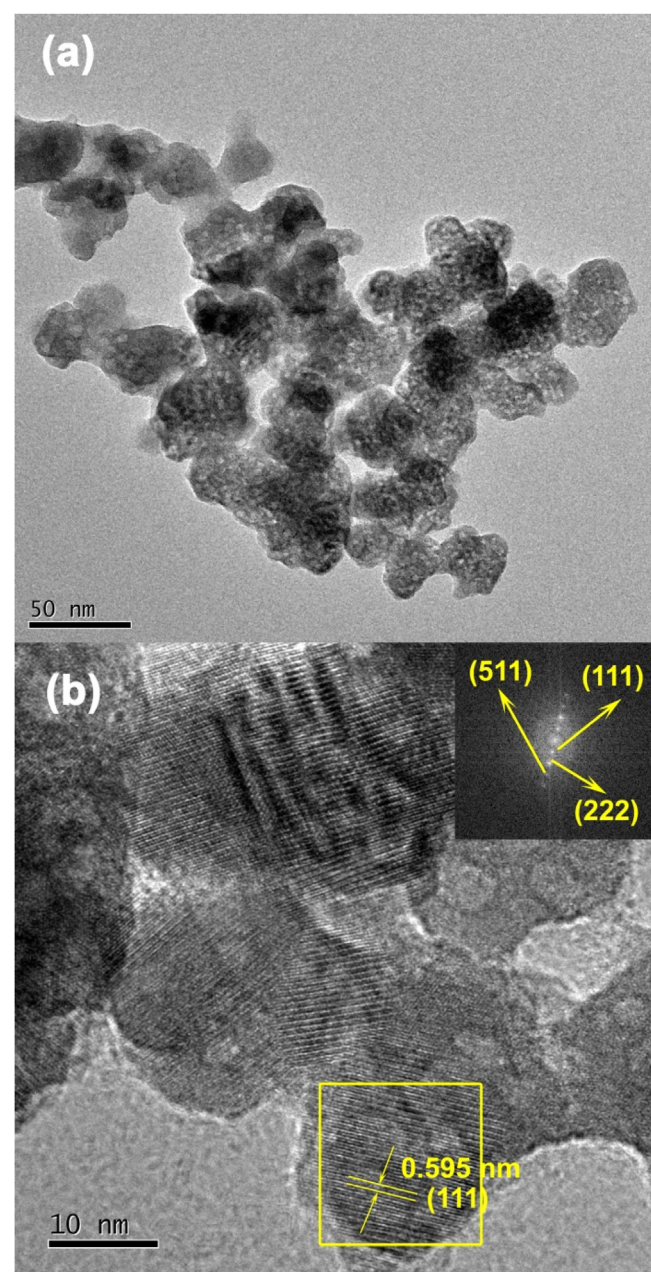


Fig. 3. TEM (a) and HRTEM (b) images of AOH, the inset in (b) is the selected-area diffraction of the area in the rectangle.

Fig. 3(a) shows a typical low-magnification TEM image of the AOH, which further exhibits that the morphology of AOH consists of irregular nanocrystals with size range from 20 nm to 50 nm. In Fig. 3(b), the clear lattice fringes of these nanocrystals indicate the high crystallinity of AOH. The interlayer spacing of 0.595 nm is corresponding to (111) of AOH. The inset of Fig. 3(b) is the fast-Fourier transformation (FFT) image of the selected area in Fig. 3(b). The bright spots represent the crystal planes (111), (222) and (511) of AOH, respectively.

The XPS spectrum of AOH is shown in Fig. 4. In the survey-scan spectra, only Sb, O and adsorbed C elements are detected (Fig. 4(a)), which is consistent with the EDS and XRD analysis. In the high-resolution XPS spectra (Fig. 4(b)), Sb 3d_{5/2} and Sb 3d_{3/2} peaks are observed at 530.2 and 539.6 eV, respectively. Furthermore, the Sb 3d_{3/2} peak presents good symmetry, thus the peak is only assignable to Sb⁵⁺ cation. The peaks of Sb 3d_{5/2} and O 1s

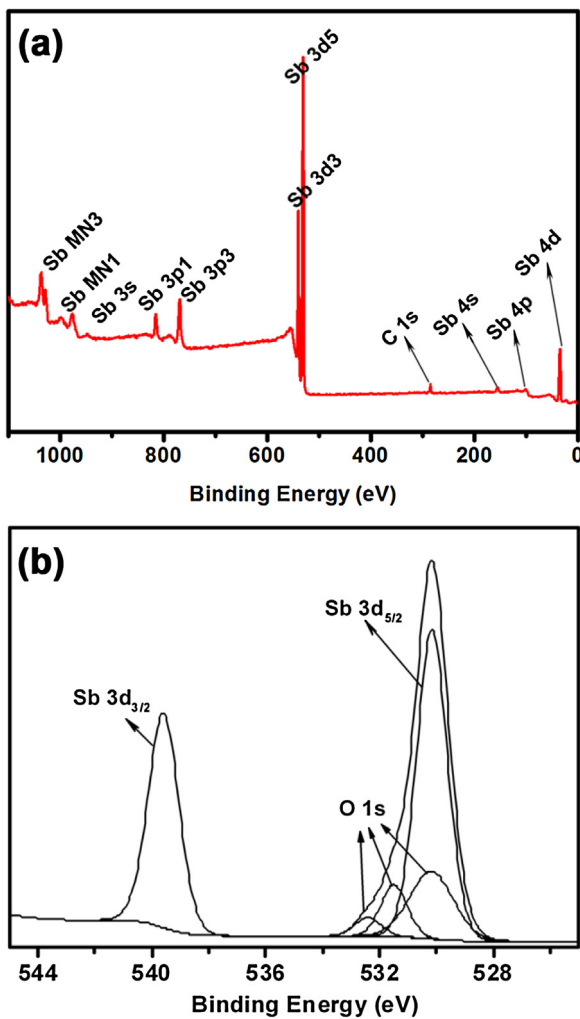


Fig. 4. Survey-scan XPS spectra of AOH (a). The High-resolution XPS spectra of Sb 3d and O 1s orbitals (b).

are overlapped at 530 eV, and we deconvolve this peak according to double-peak property of Sb 3d orbital. Therefore, the binding energy of 530.04, 531.31 and 532.41 eV are corresponding to the lattice oxygen, adsorbed oxygen and surface hydroxyl oxygen, respectively [43].

The optical property of AOH is characterized by DRS, and the spectrum is shown in Fig. 5(a). The diffuse reflectance spectrum is transformed into absorption spectrum according to the Kubelka–Munk function ($F(R) = (1 - R_\infty)^2 / 2R_\infty$), in which R_∞ is the relative reflectance of sample with infinite thickness compared with the reference. According to the relation between the absorption coefficient and band gap energy of a direct-gap semiconductor ($[F(R)E]^2 = A(E - Eg)$), the band gap of AOH is 4.1 eV. In this formula, E and Eg are the photon energy and optical band gap energy, respectively; A is the characteristic constant of semiconductors; $[F(R)E]^2$ has a linear relation with E and extrapolating the linear relation to $[F(R)E]^2 = 0$ gives the bandgap Eg of the sample. The Mott–Schottky plot of AOH is shown in Fig. 5(b). The position of conduction band could be estimated from the flat band position. For AOH, the position of flat band is estimated to be -0.29 V (vs. NHE) from the X-intercept of the linear portion of the Mott–Schottky plot. Thus, the conduction and valence band of AOH are estimated to be -0.39 V and 3.71 V (vs. NHE) [44].

The photocatalytic oxidation of gaseous benzene in a dry O_2 gas stream is carried out under UV light irradiation. Fig. 6 shows the

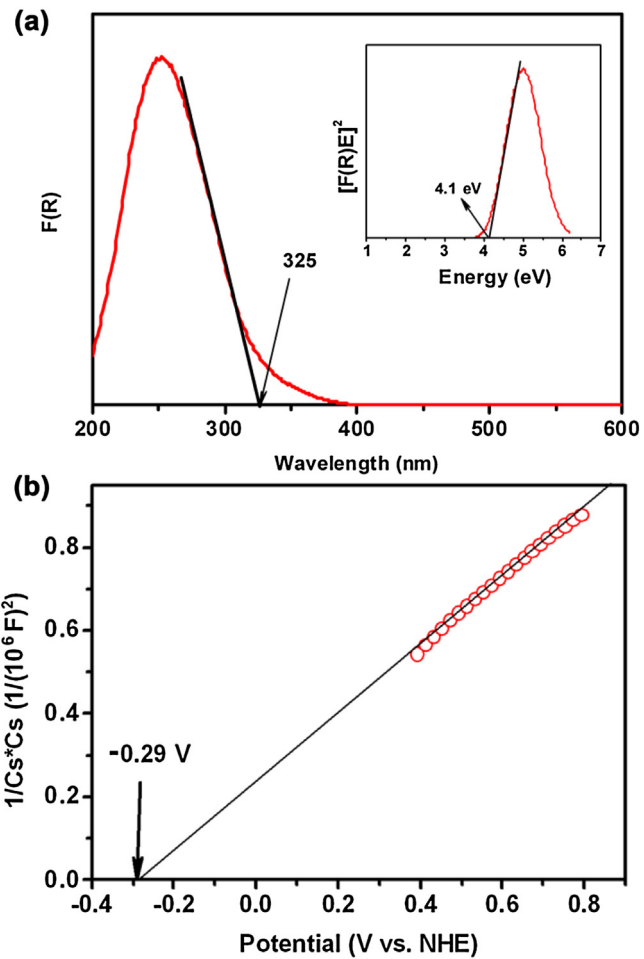


Fig. 5. UV-vis diffuse reflectance spectrum of AOH (a). Mott–Schottky plot of AOH at 1000 Hz frequency (b). The inset of (a) is the optical band gap energy Eg of AOH.

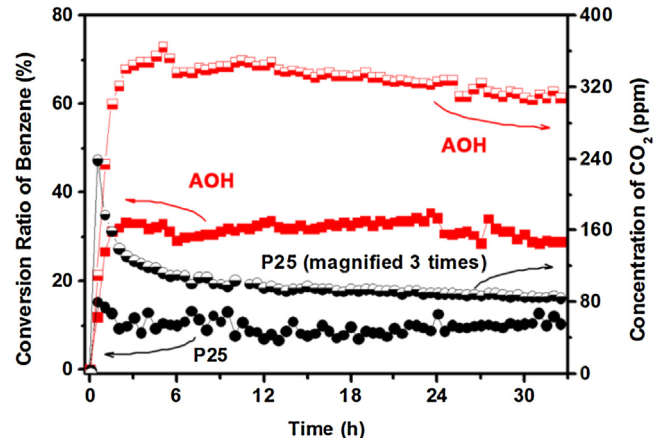


Fig. 6. The conversion ratio of benzene and concentration of CO_2 over AOH and P25.

conversion of benzene and the concentration of CO_2 over AOH and P25 as a function of time. Before irradiation, both the conversion ratio of benzene and the concentration of CO_2 are zero over either AOH or P25, which indicates that the benzene cannot be oxidized without irradiation. Photocatalytic activity of AOH is not only much higher but also more stable than that of P25 under UV light irradiation. The conversion ratio maintains 35% during the prolonged 35 h of reaction time over AOH. 340 ppm of CO_2 is produced accompanying the decomposition of benzene, which is corresponding to an

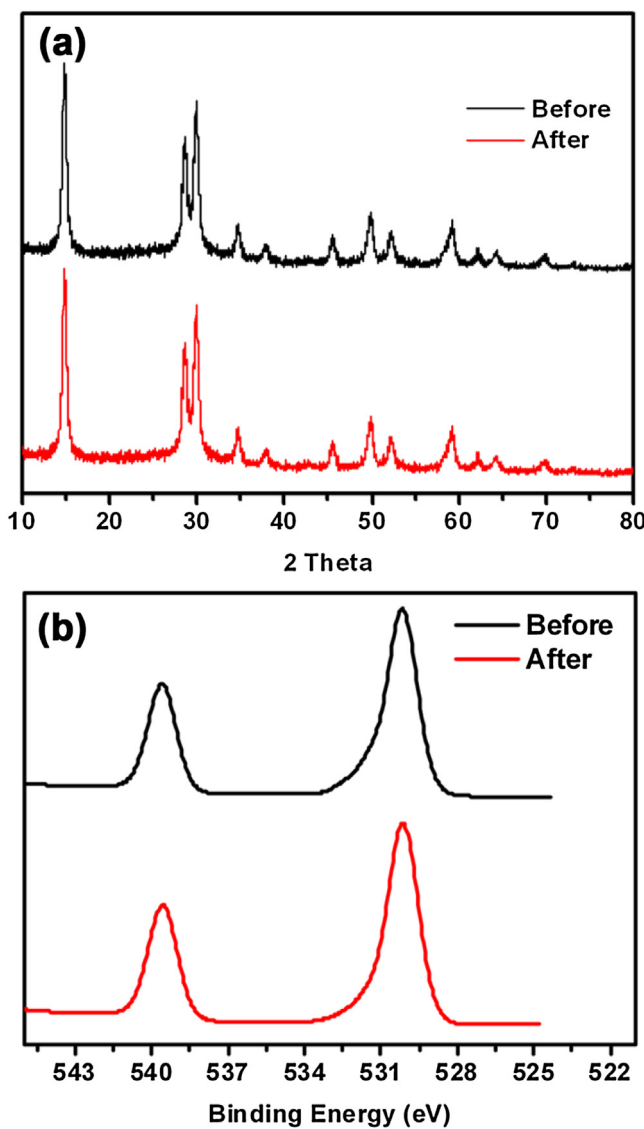


Fig. 7. The XRD (a) and XPS (b) of AOH before and after the reaction.

average mineralization ratio of 55%. In contrast to AOH, the conversion ratio of benzene over commercial P25 is 10%, accompanied by a small amount of CO_2 (26 ppm). The structure stability is also important for the photocatalyst. Therefore, the XRD and XPS are used to characterize the structure stability of the AOH. Fig. 7 illustrates that the XRD and XPS of the sample have no difference before and after the reaction indicating that the structure of the AOH is stable. We also detect the photocatalytic activity in liquid phase by oxidation of Rhodamine B (RhB) which is a compound with polycyclic chromophore. Fig. S2 shows that the photocatalytic activity for oxidation of RhB over AOH is the same with P25. To illustrate the superiority of AOH further, the controlled experiments are also conducted on the commercial samples, such as ZnO , CeO_2 and SnO_2 . Fig. S3 shows that the photocatalytic activity of AOH is better than the three commercial samples.

The variation of reaction conditions will cause the different photocatalytic activity of AOH. According to the reference, the AOH is usually synthesized at 65°C for 30 h [40], and no reference reports the best synthesized condition of AOH for photocatalytic oxidation of benzene. In this paper, the best condition for preparing AOH is studied by the orthogonal test. Three controllable variables, including the volume of H_2O_2 (mL), reaction temperature ($^\circ\text{C}$) and

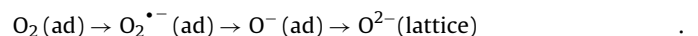
reaction time (min), are selected, each at three levels. The investigated variables and their test levels are listed in Tables S1 and S2. According to the experimental design theory, the orthogonal array $L_9(3^4)$ is selected to arrange the test program. As shown in Table S1, most of the samples do not exhibit photocatalytic activity or show very low photocatalytic activity. The XRD of the nine samples are tested. The samples No. vii–ix are Sb_2O_3 which is the raw material of the AOH. The peaks of AOH start to emerge when the volume of H_2O_2 is increased to 3 mL. However, the intensity of the peaks is very weak indicating the bad crystallinity of these samples (No. iv–vi). The sample No. i shows the best photocatalytic activity inferring that more H_2O_2 , higher temperature and longer reaction time are suitable for synthesis of the AOH.

The levels of the three factors are reset and shown in Table S2(a). The results of the orthogonal test and the extreme difference analysis are presented in Table S2(b). Obviously, the order of influence of each factors on the photocatalytic activity of benzene is $A > B > C$. The optimum levels of each factor are volume of H_2O_2 , 5 mL; Temperature, 70°C ; reaction time, 720 min. However, Table S2(b) also indicates that the reaction time has slight impact on the conversion of benzene. Therefore, the photocatalytic activity of AOH samples synthesized by 5 mL H_2O_2 at 70°C for 90 min and 720 min are compared. As presented in Fig. S4, the two samples show similar photocatalytic activity. Thus, we consider that the optimum condition for preparing AOH is volume of H_2O_2 , 5 mL; Temperature, 70°C ; reaction time, 90 min.

Particle size and BET surface area are two influence factors of photocatalytic activity. As presented in Tables S1 and S2(b), the particle size of the sample increases with the volume of H_2O_2 . When 20 mL H_2O_2 are added into the reactant, the particle size of samples are significantly larger than other samples, and their photocatalytic activity are extremely low. However, the samples synthesized with 3 mL H_2O_2 also have low activity. To further investigate the influence of H_2O_2 , the BET surfaces and the photocatalytic activity of the selected samples are tested. As shown in Table S3 and Fig. S5, the sample synthesized with 5 mL H_2O_2 exhibit the largest BET area and the best photocatalytic activity.

The amount of ROS ($\text{O}_2^{\bullet-}$ and $\bullet\text{OH}$) are detected by ESR spin trapping technique. Since the conduction band and valence band position of AOH are estimated to be -0.39 V and 3.71 V , the production of $\bullet\text{OH}$ ($\bullet\text{OH}/\text{OH}^-$ 2.38 V vs. NHE) and $\text{O}_2^{\bullet-}$ ($\text{O}_2/\text{O}_2^{\bullet-}$ -0.33 V vs. NHE) is likely to occur [45,46]. As shown in Fig. 8, the characteristic sextet peaks (Fig. 8(a)) and the quartet peaks with an intensity ratio of 1:2:2:1 (Fig. 8(b)) are observed over both AOH and P25, which are assigned to the signals of $\text{DMPO-O}_2^{\bullet-}$ and $\text{DMPO-}\bullet\text{OH}$ spin adducts [22]. The signal of $\text{DMPO-O}_2^{\bullet-}$ over AOH is much larger than P25 indicating that AOH can produce more $\text{O}_2^{\bullet-}$ than P25. The variation of $\text{O}_2^{\bullet-}$ and $\bullet\text{OH}$ with time are also investigated. The intensity of the $\text{DMPO-O}_2^{\bullet-}$ and $\text{DMPO-}\bullet\text{OH}$ signals are recorded as soon as the irradiation stops. In Fig. 8(c), the amount of $\text{O}_2^{\bullet-}$ decreases gradually over AOH, and it always larger than that of P25. In Fig. 8(d), the amount of $\bullet\text{OH}$ over AOH and P25 are the same when the light is turned off. As time goes by, the amount of $\bullet\text{OH}$ decreases sharply over the P25, while it decreases gradually over AOH. It seems that the life time of $\bullet\text{OH}$ over AOH is longer.

As shown in earlier studies, the benzene cation which is formed via addition of $\bullet\text{OH}$ is the first intermediate during benzene oxidation [47,48]. Therefore, the source of $\bullet\text{OH}$ is investigated by ESR experiments further. Generally, the adsorbed oxygen undergoes the following procedure [49]:



Among these ROS, the $\text{O}^-(\text{ad})$ can be viewed as the conjugate base of $\bullet\text{OH}$. Both of the reduction of adsorbed oxygen ($\text{O}_2(\text{ad})$) ($\text{O}_2 + \text{e}^- \rightarrow \text{O}_2^{\bullet-}$; $\text{O}_2^{\bullet-} + \text{e}^- \rightarrow \text{O}^-$) and the oxidation of lattice oxygen ($\text{O}^{2-}(\text{lattice})$) ($\text{O}^{2-}/\text{HO}^+ + \text{h}^+ \rightarrow \text{O}^-/\text{HO}^*$, trapped hole) are the

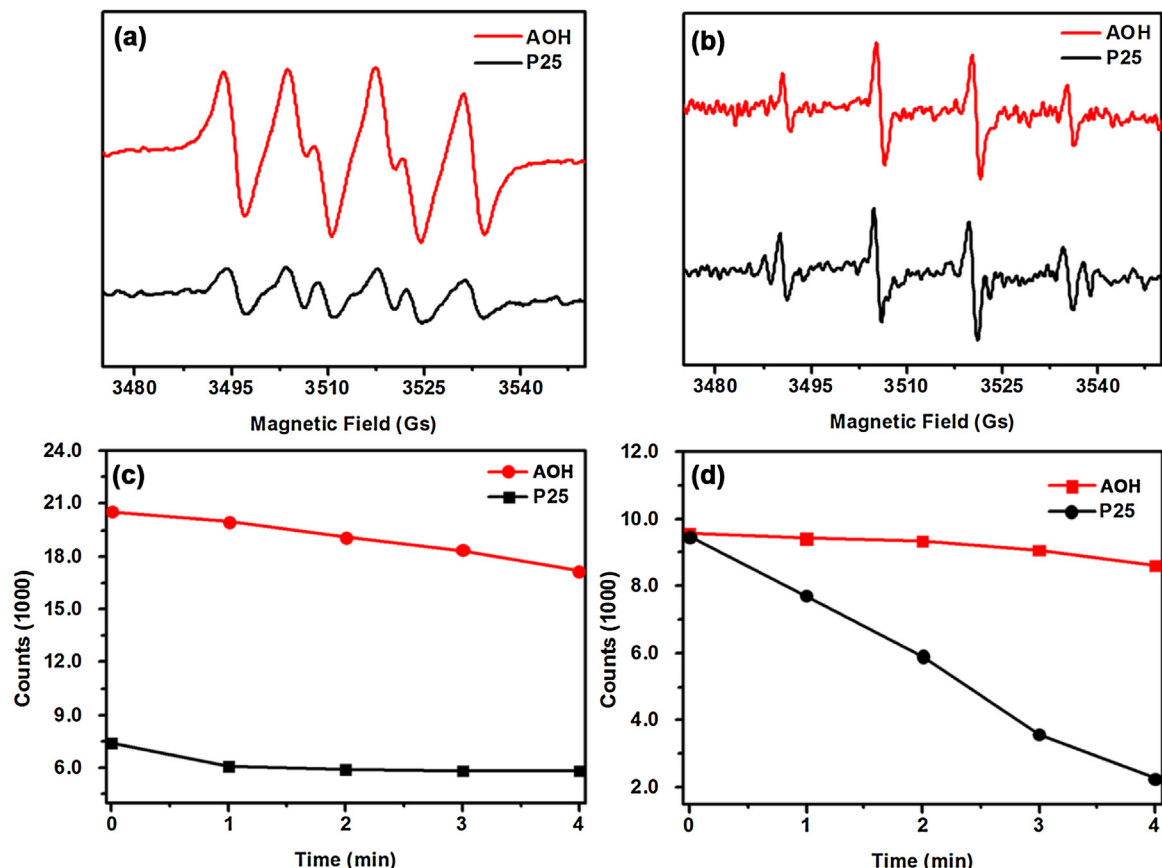


Fig. 8. The ESR signals of DMPO-O₂^{•-} (a) and DMPO-•OH (b) over AOH and P25; The variation of DMPO-O₂^{•-} (c) and DMPO-•OH (d) signal intensity with time over AOH and P25.

source of the O[−] (ad)/•OH. To distinguish the contribution of the two routes, superoxide dismutase (SOD) is used as the scavenger of O₂^{•-} to prevent the •OH from reduction of O₂ (ad) [50]. Fig. 9 shows the signals of the DMPO-•OH over AOH with or without SOD. After blocking the O₂ reduction route by SOD, the amount of •OH is largely decreased. It is considered that the decreased part of the signal results from the reduction of O₂ (ad), while the residual signal can be assigned to •OH from oxidation of O²⁻ (lattice). Predictably, •OH mainly comes from reduction of adsorbed (O₂ (ad)) through O₂^{•-}, and the large amount of O₂^{•-} (ad) is benefit for O[−] (ad)/•OH production.

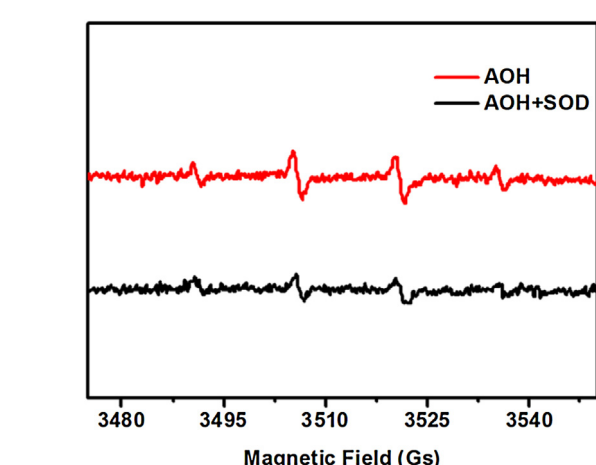
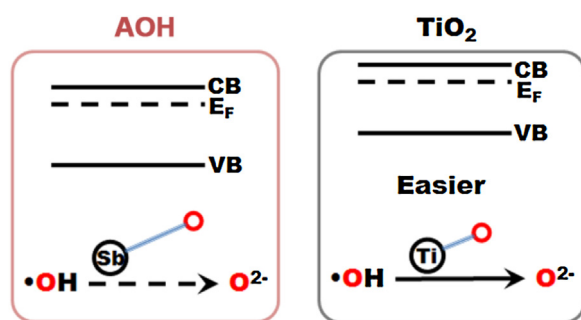


Fig. 9. The DMPO-•OH signals over AOH with or without SOD.

From what has been discussed above, the large amount of O₂^{•-} and long lived of •OH over the surface of AOH is the main reason for the good photocatalytic activity of AOH. However, the BET specific area of AOH is 38 m²/g which is smaller than that of P25 (55 m²/g) and not good for O₂ adsorption. It seems that any other property of AOH is benefit for maintaining the O₂^{•-} and •OH. The speculation is illustrated in the **Scheme 1**. From the preceding discussion, both O₂^{•-} and •OH are the products of the oxygen reduction procedure: O₂ (ad) → O₂^{•-} (ad) → O[−] (ad) → O²⁻ (lattice). Moreover, the products of oxygen reduction can be influenced by the reducibility of a semiconductor according to the previous work [51]. From Fig. 5(b), the conduction band of AOH is −0.39 V, which is lower than that of P25 (−0.6 V vs. NHE, (Fig. S6)) [52]. Therefore, reaction between e[−] and O₂ is easier over P25, and the procedure of the oxygen



Scheme 1. The speculation of oxygen reduction over AOH and P25. The blue bar represents the bond between metal and oxygen. (For interpretation of the references to colour in this scheme legend, the reader is referred to the web version of this article.)

reduction moving to the O^{2-} (lattice) direction is also speculated to be easier. On the other hand, the bond length of metal–oxygen (M–O) is used to illustrate the stability of the M–O bond. The shorter bond length means the larger bond energy and more stable O^{2-} (lattice). On the surface of TiO_2 , the bond length of Ti–O is 1.909 Å, while in the bulk of AOH the bond length of Sb–O is 1.98 Å [53,54]. The Sb–O data on the surface is not found, but it is deduced larger than the data in the bulk. Thus, the O^{2-} (lattice) is less stable on the surface of AOH, which is benefit for maintaining the $O_2^{•-}$ and $•OH$.

4. Conclusions

In this paper, we use a facile hydrolysis–oxidation method to prepare the antimony oxide hydrate (AOH) photocatalyst containing only one metal. By tuning the temperature, length of time and the volume of H_2O_2 , we find that the AOH adopts the pyrochlore phase in a wide range of reaction condition. The sample with the best photocatalytic activity is synthesized at 70 °C for 90 min with 5 mL H_2O_2 . The photocatalytic activity for oxidation of benzene over this photocatalyst is investigated for the first time. The conversion ratio of benzene is 35.0% with about 340 ppm of CO_2 produced, corresponding to an average mineralization ratio of 55%. The conversion ratio and the mineralization ratio are 3.5 and 5.5 times higher than that of P25. Reactive oxygen species, including $O_2^{•-}$ and $•OH$, are detected by ESR experiments. The large amount of $O_2^{•-}$ and long lived of $•OH$ over the surface of AOH is the main reason for its good photocatalytic activity. We also prove that both $O_2^{•-}$ and $•OH$ are mainly origin from oxygen reduction. We believe that this simple and high efficient photocatalyst has potential industrial application value.

Acknowledgement

This work was financially supported by the NNSF of China (21173047 and 21373049).

Appendix A. Supplementary data

Supplementary data associated with this article can be found, in the online version, at <http://dx.doi.org/10.1016/j.apcatb.2017.04.004>.

References

- [1] J. Wilbourn, L. Haroun, E. Heseltine, J. Kaldor, C. Partensky, H. Vainio, *Carcinogenesis* 7 (1986) 1853–1863.
- [2] X.Z. Fu, W.A. Zeltner, M.A. Anderson, *Appl. Catal. B Environ.* 6 (1995) 209–224.
- [3] Y. Liu, L. Wang, W. Jin, C. Zhang, M. Zhou, W. Chen, *J. Alloys Compd.* 690 (2017) 604–611.
- [4] S. Weon, W. Choi, *Environ. Sci. Technol.* 50 (2016) 2556–2563.
- [5] X. Wang, Q. Ni, D. Zeng, G. Liao, C. Xie, *Appl. Surf. Sci.* 389 (2016) 165–172.
- [6] L. Ren, M. Mao, Y. Li, L. Lan, Z. Zhang, X. Zhao, *Appl. Catal. B Environ.* 198 (2016) 303–310.
- [7] M.C. Lin, J.C. Kao, *Mar. Pollut. Bull.* 105 (2016) 139–142.
- [8] J. Li, X. Liu, Z. Sun, L. Pan, *J. Colloid Interface Sci.* 463 (2016) 145–153.
- [9] H. Lin, J. Long, Q. Gu, W. Zhang, R. Ruan, Z. Li, X. Wang, *Phys. Chem. Chem. Phys.* 14 (2012) 9468–9474.
- [10] C. Zhao, Y. Song, Y. Yang, W. Chen, X. Li, Z. Wang, *Funct. Mater. Lett.* 08 (2015) 1550071.
- [11] A.O. Kondrakov, A.N. Ignatev, V.V. Lunin, F.H. Frimmel, S. Bräse, H. Horn, *Appl. Catal. B Environ.* 182 (2016) 424–430.
- [12] H. Huang, G. Liu, Y. Zhan, Y. Xu, H. Lu, H. Huang, Q. Feng, M. Wu, *Catal. Today* 281 (2017) 649–655.
- [13] N.S. Andryushina, O.L. Stroyuk, *Appl. Catal. B Environ.* 148–149 (2014) 543–549.
- [14] Y. Ma, Y. Li, M. Mao, J. Hou, M. Zeng, X. Zhao, *J. Mater. Chem. A* 3 (2015) 5509–5516.
- [15] F. He, J. Li, T. Li, G. Li, *J. Chem. Eng. Data* 237 (2014) 312–321.
- [16] L. Ren, Y. Li, J. Hou, J. Bai, M. Mao, M. Zeng, X. Zhao, N. Li, *Appl. Catal. B Environ.* 181 (2016) 625–634.
- [17] M. Zeng, Y. Li, M. Mao, J. Bai, L. Ren, X. Zhao, *ACS Catal.* 5 (2015) 3278–3286.
- [18] J. Mo, Y. Zhang, Q. Xu, J.J. Lamson, R. Zhao, *Atmos. Environ.* 43 (2009) 2229–2246.
- [19] M. Gholami, H.R. Nassehnia, A. Jonidi-Jafari, S. Nasseri, A. Esrafili, *J. Environ. Health Sci. Eng.* 12 (2014) 45.
- [20] J.F. Montoya, I. Ivanova, R. Dillert, D.W. Bahnemann, P. Salvador, J. Peral, *J. Phys. Chem. Lett.* 4 (2013) 1415–1422.
- [21] X. Fu, J. Wang, D. Huang, S. Meng, Z. Zhang, L. Li, T. Miao, S. Chen, *ACS Catal.* 6 (2016) 957–968.
- [22] J. Wang, H. Li, S. Meng, L. Zhang, X. Fu, S. Chen, *Appl. Catal. B Environ.* 200 (2017) 19–30.
- [23] J. Huang, K. Ding, X. Wang, X. Fu, *Langmuir* 25 (2009) 8313–8319.
- [24] M. Sun, D. Li, Y. Zheng, W. Zhang, Y. Shao, Y. Chen, W. Li, X. Fu, *Environ. Sci. Technol.* 43 (2009) 7877–7882.
- [25] S. Meng, D. Li, M. Sun, W. Li, J. Wang, J. Chen, X. Fu, G. Xiao, *Catal. Commun.* 12 (2011) 972–975.
- [26] D. Huang, X. Fu, J. Long, X. Jiang, L. Chang, S. Meng, S. Chen, *Chem. Eng. J.* 269 (2015) 168–179.
- [27] Y. Luo, J. Chen, J. Liu, Y. Shao, X. Li, D. Li, *Appl. Catal. B Environ.* 182 (2016) 533–540.
- [28] M. Sun, D. Li, W. Zhang, Z. Chen, H. Huang, W. Li, Y. He, X. Fu, *J. Solid State Chem.* 190 (2012) 135–142.
- [29] Z. Li, Z. Xie, Y. Zhang, L. Wu, X. Wang, X. Fu, *J. Phys. Chem. C* 111 (2007) 18348–18352.
- [30] M. Sun, D.Z. Li, W.J. Zhang, X.Z. Fu, Y. Shao, W.J. Li, G.C. Xiao, Y.H. He, *Nanotechnology* 21 (2010).
- [31] R.J. Jitta, R. Gundebolina, N.K. Veldurthi, R. Guje, V. Muga, *J. Chem. Technol. Biotechnol.* 90 (2015) 1937–1948.
- [32] Z. Yi, J. Ye, N. Kikugawa, T. Kako, S. Ouyang, H. Stuart-Williams, H. Yang, J. Cao, W. Luo, Z. Li, Y. Liu, R.L. Withers, *Nat. Mater.* 9 (2010) 559–564.
- [33] Y. Liu, W. Yao, D. Liu, R. Zong, M. Zhang, X. Ma, Y. Zhu, *Appl. Catal. B Environ.* 163 (2015) 547–553.
- [34] J. Fang, D. Li, Y. Shao, J. Hu, *J. Mater. Chem. A* 4 (2016) 14213–14221.
- [35] J. Wang, H. Ruan, W. Li, D. Li, Y. Hu, J. Chen, Y. Shao, Y. Zheng, *J. Phys. Chem. C* 116 (2012) 13935–13943.
- [36] Y. Hu, D. Li, Y. Zheng, W. Chen, Y. He, Y. Shao, X. Fu, G. Xiao, *Appl. Catal. B Environ.* 104 (2011) 30–36.
- [37] H.J. Huang, D.Z. Li, Q. Lin, W.J. Zhang, Y. Shao, Y.B. Chen, M. Sun, X.Z. Fu, *Environ. Sci. Technol.* 43 (2009) 4164–4168.
- [38] Y. Hou, X. Wang, L. Wu, Z. Ding, X. Fu, *Environ. Sci. Technol.* 40 (2006) 5799–5803.
- [39] J. Chen, Y. Shao, D. Li, *J. Mater. Chem. A* 5 (2017) 937–941.
- [40] J. Shi, L. Ma, P. Wu, Z. Zhou, P. Guo, S. Shen, D. Jing, L. Guo, *Nano Res.* 5 (2012) 576–583.
- [41] J. Wang, K. Ozawa, M. Takahashi, M. Takeda, T. Nonami, *Chem. Mater.* 18 (2006) 2261–2264.
- [42] N. Yang, G. Li, X. Yang, W. Wang, W.F. Zhang, *Dalton Trans.* 40 (2011) 3459–3461.
- [43] G. Lu, S.L. Bernasek, J. Schwartz, *Surf. Sci.* 458 (2000) 80–90.
- [44] T. Zhu, M.N. Chong, E.S. Chan, *ChemSusChem* 7 (2014) 2974–2997.
- [45] H.-i. Kim, H.-n. Kim, S. Weon, G.-h. Moon, J.-h. Kim, W. Choi, *ACS Catal.* 6 (2016) 8350–8360.
- [46] W. Li, D. Li, S. Meng, W. Chen, X. Fu, Y. Shao, *Environ. Sci. Technol.* 45 (2011) 2987–2993.
- [47] H. Einaga, *Appl. Catal. B Environ.* 38 (2002) 215–225.
- [48] O. d’Hennezel, P. Pichat, D.F. Ollis, C. Belver, *J. Photochem. Photobiol. A* 118 (1998) 197–204.
- [49] G. Zou, Y. Xu, S. Wang, M. Chen, W. Shangguan, *Catal. Sci. Technol.* 5 (2015) 1084–1092.
- [50] W. He, H.K. Kim, W.G. Wamer, D. Melka, J.H. Callahan, J.J. Yin, *J. Am. Chem. Soc.* 136 (2014) 750–757.
- [51] K. Morita, K. Sakuma, K. Miyajima, F. Mafune, *J. Phys. Chem. A* 117 (2013) 10145–10150.
- [52] T. Giannakopoulou, I. Papailias, N. Todorova, N. Boukos, Y. Liu, J. Yu, C. Trapalis, *Chem. Eng. J.* 310 (2017) 571–580.
- [53] P. Raghunath, W.F. Huang, M.C. Lin, *J. Chem. Phys.* 138 (2013) 154705.
- [54] K. Ozawa, M. Hase, H. Fujii, M. Eguchi, H. Yamaguchi, Y. Sakka, *Electrochim. Acta* 50 (2005) 3205–3209.